A Ritz approach for the static analysis of planar pantographic structures modeled with nonlinear Euler-Bernoulli beams

Ugo Andreaus · Mario Spagnuolo · Tomasz Lekszycki · Simon R. Eugster

Abstract We present a finite element discrete model for pantographic lattices, based on a continuous Euler-Bernoulli beam for modeling the fibers composing the pantographic sheet. This model takes into account large displacements, rotations and deformations; the Euler-Bernoulli beam is described by using non-linear interpolation functions, a Green-Lagrange strain for elongation and a curvature depending on elongation. On the basis of the introduced discrete model of a pantographic lattice, we perform some numerical simulations. We then compare the obtained results to an experimental BIAS extension test on a pantograph printed with polyamide PA2200. The pantographic structures involved in the numerical as well as in the experimental investigations are not proper fabrics: they are composed by just a few fibers for theoretically allowing the use of the Euler-Bernoulli beam theory in the description of the fibers. We compare the experiments to numerical simulations in which we allow the fibers to elastically slide one respect to

Corresponding Author: mario.spagnuolo@lspm.cnrs.fr

Ugo Andreaus
Università di Roma “La Sapienza”, Roma, Italy.
E-mail: ugo.andreaus@uniroma1.it

Mario Spagnuolo
CNRS, LSPM UPR3407, Université Paris 13, Sorbonne Paris Cité, 93430 Villetaneuse, France.
International Research Center M&MoCS, Università degli Studi dell’Aquila. Via Giovanni Gronchi 18 - Zona industriale di Pile, 67100 L’Aquila, Italy.
E-mail: mario.spagnuolo@lspm.cnrs.fr

Tomasz Lekszycki
International Research Center M&MoCS, Università degli Studi dell’Aquila. Via Giovanni Gronchi 18 - Zona industriale di Pile, 67100 L’Aquila, Italy.
Institute of Mechanics and Printing, Warsaw University of Technology. 85 Narbutta Street, 02-524 Warsaw, Poland.
Department of Experimental Physiology and PAthophysiology, Medical University of Warsaw. 1b Banacha Street, 02-097 Warsaw, Poland.
E-mail: t.lekszycki@wip.pw.edu.pl

Simon R. Eugster
Universität Stuttgart, Stuttgart, Institute for Nonlinear Mechanics (INM).
E-mail: eugster@inm.uni-stuttgart.de

the other in correspondence of the interconnecting pivot. We present as result a very good agreement between the numerical simulation, based on the introduced model, and the experimental measures.

Keywords pantographic structures · non-linear Euler-Bernoulli beam · Ritz method · finite element method

1 Introduction

In this paper we want to present a numerical model to predict the global behaviour under deformation of pantographic structures which are composed by some fibers, arranged in a particular way we will precisely describe, modeled as non-linear Euler-Bernoulli beams. In this paper we consider the deformations of a pantograph as the one in Fig. 1. The pantographic structure we want to model

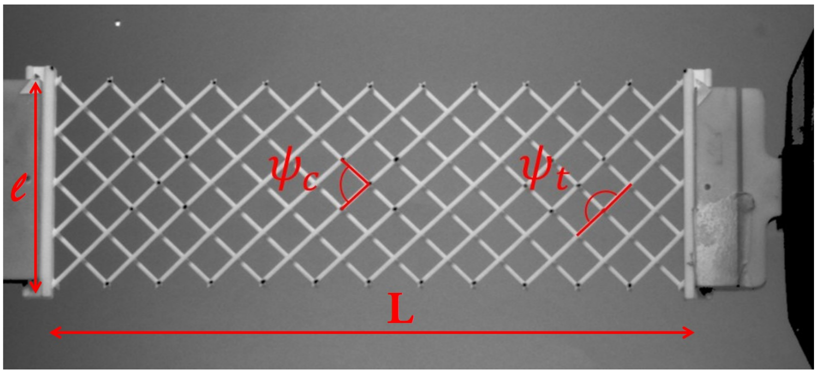

Fig. 1 Specimen in the reference configuration.

Properties of the sample	
Material	Polyamide PA2200
ℓ	$0.07\,m$
L	$0.21\,m$
Pivot height	$3\,mm$
Pivot radius	$0.5\,mm$

Table 1 Properties of the sample used in the experiment

corresponds to a real 3D printed rectangular specimen (of dimensions ℓ and L, see Fig. 1) consisting in a planar grid constituted by two families of continuous fibers orthogonally intersecting and connecting each other in nodes which we call pivots (the pivots do not interrupt the continuity of the fibers). Each fiber belonging to one, say "A", of the two arrays is connected by the pivots to the fibers belonging to the other array, say "B". Notice that each fiber is continuous throughout all its length. The two families of fibers intersect the sides of the rectangular shape at an angle of $\pm 45^o$ in the initial configuration. The real pivots are cylinders whose torsion and flexion are *a priori* non negligeable. The total number of pivots (say, nodes) is N_p and the toat number of segments (say, elements or members) comprised between two pivots is M. The experimental values of the properties of the sample are reported in Tab. 1.

The model we use consists in a sort of "meso-model" between the discrete mass-spring model used as a reference in [1] (see [2] for applications in case of dynamical regimes) and the homogenised one (see again [1]). Some useful properties of non-linear elastic systems, as stability and particular typologies of deformation (buckling, etc...), are reported in [3]. We consider here the non-linear Euler-Bernoulli beam theory, which takes into account large displacements, rotations and deformations. To perform the numerical calculation and obtain the solution we use a Ritz approach discretization, by considering as finite element the part of beam between two consecutive pivots of a same beam. We lastly model the pivot itself via a torsional spring and an extensional spring which allows the sliding of a fiber respect another of the other family in correspondence of the interconnecting pivot.

A review on models for pantographic fabrics is presented in [4]. A second gradient formulation for a 2D fabric sheet with inextensible fibres is also possible, as shown in [5–7]. Preliminary studies about pantographic 2D lattices with internal pivots can be found in the pioneering work [8]. A discrete spring model for extensible beams is considered and a heuristic homogenization technique is proposed to formulate a continuum fully nonlinear beam model in [1, 9]. In [10], a system constituted by a large number of beams interconnected via ideal hinges is considered, and some numerical simulations concerning the static and dynamic analysis of the system are presented and discussed as the number of beams increases. In [11] it was considered a bi-dimensional sheet consisting of two orthogonal families of inextensible fibres, and numerically simulated a standard bias extension test on the sheet, solving a non-linear constrained optimization problem. Several first and second gradient deformation energy models were considered, depending on the shear angle between the fibres and on its gradient, and the results obtained were compared. In [12] it was presented a novel numerical code implementing directly the discrete Hencky-type model which is robust enough to solve the problem of the determination of equilibrium congurations in the large deformation and displacement regimes. The fact that the pivots interconnecting the two arrays of beams may store elastic energy was efficiently modeled introducing suitable "torsional" springs. The problem of determining equilibrium congurations is successively solved by imposing the stationarity of total potential energy of the system. The first available experimental evidence obtained for sheared pantographic specimens is shown in [13] where how effective and predictive is the aforementioned code [12] is also shown. Subsequently, a simple fiber rupture mechanism is postulated and added to the initially elastic model. In [14] it has been studied how the mechanical properties of pantographic structures are affected by statistically distributed defects. The relevance of the treated problem is more cogent as the technological tools now available allow for the construction of more and more miniaturised fabrics constituted by beam lattices. In [15] it has been approached a study about buckling patterns in pantographic sheets, regarded as two-dimensional continua consisting of lattices of continuously distributed fibers. The fibers are modeled as beams endowed with elastic resistance to stretching, shearing, bending and twist. Included in the theory is a non-standard elasticity due to geodesic bending of the fibers relative to the lattice surface. It is possible to model such structures at a suitably small length scale (resolving in detail the interconnecting pivots/cylinders) using a microscopic model which is a quadratic isotropic Saint-Venant first gradient continuum including geometric nonlinearities and characterized by two Lamè parameters. The introduced macroscopic two-dimensional model for pantographic sheets is characterized by a deformation energy quadratic both in the first and second gradient of placement. Moreover, it is needed that the second gradient stiffness depends on the first gradient of placement if large deformations and large displacements configurations must be described. The numerical identification procedure consists in fitting the macro-constitutive parameters using several numerical simulations performed with the micro-model.

In the same family of the previous cited microstructured (meta-)materials it is possible to introduce also different kind of microstructures (see for example [16–19]) which can be enriched by using some homogenisation procedure, as in [20, 21], also performed by numerical tools [21]. Via homogenisation procedures one in general obtains higher gradient continua [22, 23]: in some particular cases the more specific second gradient continua are obtained, as in [24–28], where the properties of second gradient material are produced by the specific microstructure (in [27], for example, the authors start from a linear elastic truss, which is an interesting case if compared to pantographic structures, studied in the present paper).

The aim of this paper is to find a predictive model for global deformations of pantographic structures. The interest in these meta-materials was increased by the possibilities opened by the diffusion of technology of three-dimensional printing.

The system considered herein was first investigated in [8,29], where simulations about linearized behavior were shown. The proposed numerical simulations will be helpful in designing a systematic experimental campaign aimed at characterizing the internal energy for physical realizations of the ideal pantographic structure presented in this paper.

In section 2 we present the real physical system and the model we use to describe it. In section 3 a short introduction on the non-linear Euler-Bernoulli beam theory is given. In section 4 we write the total potential energy of a pantographic structure modeled by using the non-linear Euler-Bernoulli beam theory and its discretization via a Ritz approach is given in section 5. Section 6 introduces a first application of the code developed by using the results presented in the previous sections. Here we consider the simplest structures possible: the modules X and XX. In section 7 we present numerical simulations relative to an extension test we also performed on a real 3D printed pantograph. In this section we also compare the numerical results with the experiments. In section 8 we discuss about some qualitative results we can derive from numerical simulations. Section 9 briefly concludes.

2 The model

The real system we described is analysed via a mechanical model, whose reference configuration $\mathcal{C}^*$ is graphically represented in Fig. 2. The fibers, divided in the two families "A" and "B", are contained in a rectangle whose dimensions in $\mathcal{C}^*$ are ℓ and L, which are in a proportionality relation $L = g\ell$. For the numerical

System	
N_p number of pivots	109
N_f number of fibers	30
M number of finite elements	96
Cross-section area	$144 \cdot 10^{-8}\, m^2$
Cross-section inertia moment	$9.72 \cdot 10^{-14}\, m^4$
Youngs modulus	$1600 \cdot 10^6\, Pa$

Table 2 Geometrical properties

values one can refer to Tabs. 1-2. Each member of length L_i comprised between two nodes is modeled as a Euler-Bernoulli beam and therefore is endowed with a stretching energy W_s^i and a bending energy W_b^i, respectively related to axial strain ϵ at centroid axis and bending strain κ of a shear undeformable beam, as it will be shown in the following.

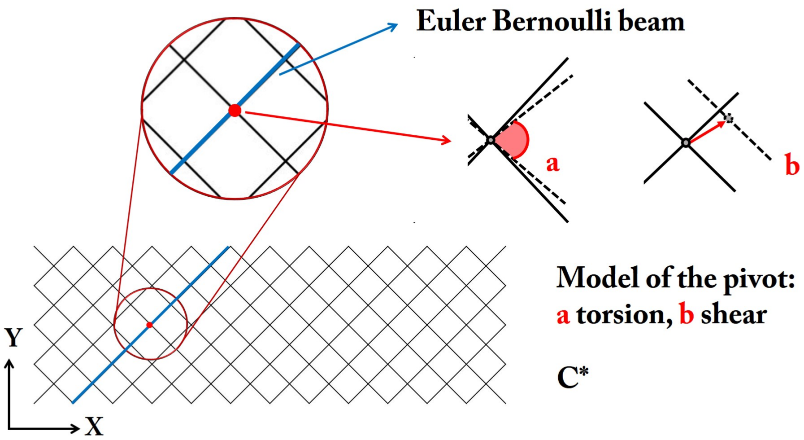

Fig. 2 Graphical representation of the reference configuration and model of the pivot.

For describing a real pantographic sheet we are obliged to introduce an energetic term related to the torsion of the pivots (at the micro-level, while, at the macro-homogenized-level, it has to be related to the shear in the pantographic sheet, as in [1]). Following the *ansatz* presented in [30], we add a term in order to take into account the possibility that fibers of different families slide one respect to the other in correspondence of a pivot (which in a micro description of the problem can be interpreted as the energy relative to the flexion or the shear of the pivot, Fig. 3). In the following sections we will need to identify the pivots and the finite elements composing the single Euler-Bernoulli beams: for this aim we refer to Fig. 4 for the numbering.

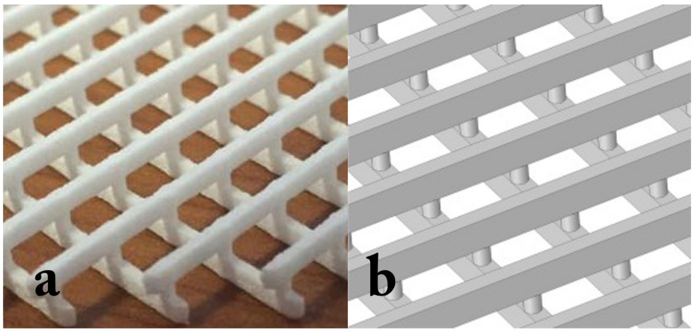

Fig. 3 Image of real pivots (a) and computer representation (b).

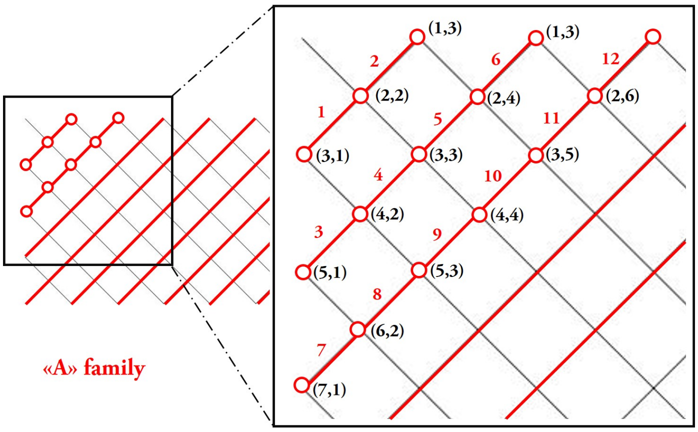

Fig. 4 Description of numbering process for family A. We identify the pivots by a couple of numbers (as if the pivots were disposed as the elements of a matrix) and the finite elements by just one number. A similar description can be done for the family B.

3 Potential energy of the pantographic structure

The modeling procedure is to be completed by defining the deformation energy. The problem of determining equilibrium configurations is successively solved by imposing the stationarity of total potential energy. Consider the energy for a single member i, whose length is L_i $(i = 1, \dots, M)$: each beam stores elastically an energy which depends quadratically on variations of its length, Eq. (42), (stretching energy)

$$W_s = \sum_{i=1}^{M} \frac{1}{2} \int_0^{L_i} EA\epsilon^2 \, dx \tag{1}$$

and curvature, Eq. (46), (bending energy)

$$W_b = \sum_{i=1}^{M} \frac{1}{2} \int_0^{L_i} EI\kappa^2 \, dx \tag{2}$$

for the system composed by all the members, whose total number is M.

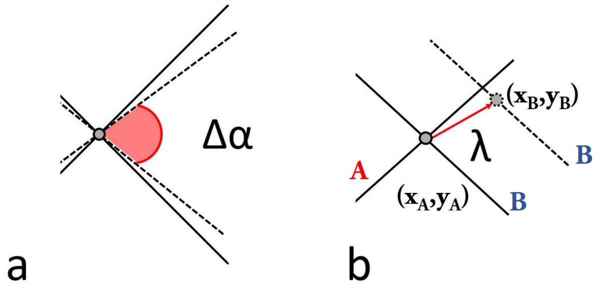

Fig. 5 Representation of pivot energetic terms.

By referring to Fig. 5.a we write pivot torsion energy as follows

$$W_p = \sum_{i=1}^{N_p} \frac{1}{2} k_p \left(\frac{\pi}{2} - \Delta\alpha_i \right)^2 \tag{3}$$

$\Delta\alpha_i$ is the angle change between the current chord $i_c - j_r$ with respect to the reference chord $i_c - j_t$ (Fig. 6).

A last energetic contribution has to be added. By referring to Fig. 5.b, we write the interaction energy as

$$W_f = \sum_{i=1}^{N_p} \frac{1}{2} k_f (\lambda_i^2 + k_3 \lambda_i^3 + \dots) \tag{4}$$

where $\lambda = \sqrt{[(X_A + U_A) - (X_B + U_B))]^2 + [(Y_A + V_A) - (Y_B + V_B))]^2}$, with (X_A, Y_A) and (X_B, Y_B) the coordinates of the points of the two families corresponding to a same pivot in the reference system of the undeformed configuration and U_A, U_B, V_A and V_B the nodal displacements. In general we can have a nth order polynomial in λ. In the following we will use only the λ_2 and λ_3 terms, which allow together to fit both the force-displacement experimental plot and the deformed shape of the pantograph.

Then we have

$$W = W_s + W_b + W_p + W_f \tag{5}$$

for the total energy W of the structure. We postulate the axiome of minimum of potential energy to get the equilibrium condition

$$\delta W = 0 \tag{6}$$

which has to hold for all admissible virtual displacements compatible with the specified boundary conditions.

4 Discretization by a Ritz approach

We cannot solve analytically the presented problem. For this reason, we propose a Ritz approach by distretizing the energy and by introducing some shape functions to describe the displacements. The beam segment comprised between two nodes will be referred to in the following as "local beam" or simply "element" or "member"; the total number of (free, fixed, actioned) nodes is N_p and the total number of elements is M. The k-th element is shown in Fig. 6, where i and j are the end nodes of the element, $X-Y$ is the fixed global reference system, X_i, Y_i are the coordinates of the node i in the fixed reference $X-Y$, $x-y$ is the moving local reference system; in the finite element grid formulation, the latter one is rigidly bounded to the line segment $i-j$ in the initial configuration and to the line segment $i_c - j_c$ in the current configuration. If the element displaces as a rigid body, the local reference axes are carried with it and no element deformations are induced. Relative to this reference system, the element can be visualized as a

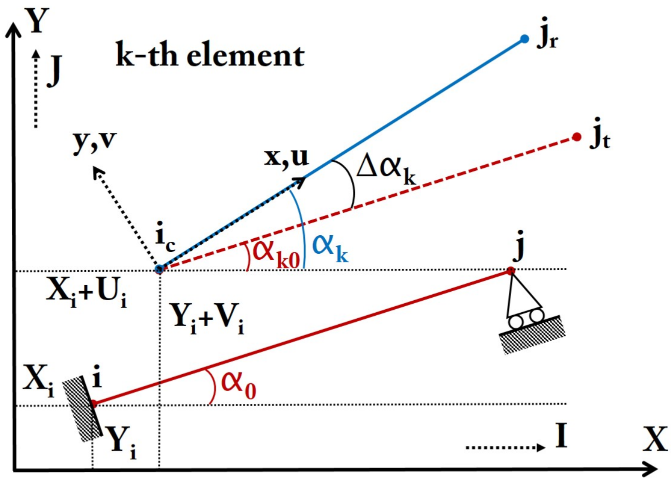

Fig. 6 Global and local reference systems and rigid-body motions of the single grid element.

simply supported beam with a pin at nodes i and i_c, and with a roller at nodes j, j_t and j_r. This virtual supporting system simply allows to suppress the rigid body modes. The kinematics of this generic element moving from its initial (reference) to current configuration is described by its nodal displacements in the fixed global reference system (X-Y), Fig. 6, in accord to the work [31]. These nodal generalized displacements are: U_i, U_i', V_i, Φ_i, U_j, U_j',V_j, Φ_j, where U_i, V_i, U_j, V_j are translations of nodes i and j respectively in the fixed reference system $X-Y$, Φ_i, Φ_j total rotations and U_i', U_j' first derivatives of axial displacement. As shown in Fig. 7 the basic element deformations are defined as displacements relative to the local reference axes $x-y$. In sum, the nodes i and j represent the initial configuration, the nodes i_c and j_t, j_r rigid body motions (translation, i_c, j_t, and rotation, j_r, respectively), the nodes i_c and j_c deformations (extension and flexure). Let the rectilinear line segment connecting nodes i_c and j_c be defined "current chord"; the element deformations of this basic system are defined as: (1) the relative displacement δ_k of the node j_c with respect to the node j_r along the current chord; (2) the rotation φ_i of the tangent line at node i_c and (3) the rotation φ_j of the tangent line at node j_c relative to the current chord. Thus, these three basic element

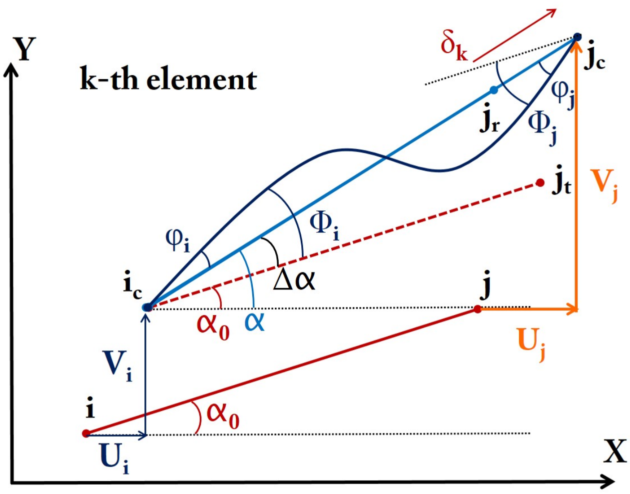

Fig. 7 Kinematics and deformations of the single grid element.

deformations are defined as

$$\delta_k = L_k - L_{k0} \tag{7}$$

$$\varphi_i = \Phi_i - (\alpha_k - \alpha_{k0}) = \Phi_i - \Delta\alpha_k \tag{8}$$

$$\varphi_j = \Phi_j - (\alpha_k - \alpha_{k0}) = \Phi_j - \Delta\alpha_k \tag{9}$$

where L_{k0} and L_k are the initial and current lengths of k-th element reference $(i - j)$ and current (i_c-j_c) chords, respectively and are computed as

$$L_{k0} = \sqrt{(X_j - X_i)^2 + (Y_j - Y_i)^2} \tag{10}$$

$$L_k = \sqrt{[(X_j + U_j) - (X_i + U_i)]^2 + [(Y_j + V_j) - (X_i + V_i)]^2} \tag{11}$$

in terms of the initial $X - Y$ coordinates and nodal displacements U, V in the fixed reference $X - Y$.

The angles α_{k0} and α_k denote the orientations of initial $i - j$ and current $i_c - j_c$ element chords in the global system, respectively, and are expressed as

$$\alpha_{k0} = \arctan\left(\frac{Y_j - Y_i}{X_j - X_i}\right) \tag{12}$$

$$\alpha_k = \arctan\left\{\frac{[(Y_j + V_j) - (Y_i + V_i)]}{[(X_j + U_j) - (X_i + U_i)]}\right\} \tag{13}$$

$\Delta\alpha_k$ denotes the rigid body rotation of the element reference $i - j$ to the current $i_c - j_c$ chord

$$\Delta\alpha_k = \alpha_k - \alpha_{k0} \tag{14}$$

The continuity condition in the i node common to two connected beam elements, say k and $k + 1$, belonging to the same family, states that

$$U_{k,j} = U_{k+1,i} \tag{15}$$

$$V_{k,j} = V_{k+1,i} \tag{16}$$

$$\Phi_{k,j} = \Phi_{k+1,i} \tag{17}$$

Due to the order of the derivatives appearing in Eqs. (44-47), the axial displacement u and transverse displacement v require, at least, functions with continuity C^2. Therefore, in the local reference system $x - y$ (see Fig. 6) the generalized displacements (u, v) inside the element are interpolated from the (nodal) local displacements using the expressions

$$u = H_3\delta + H_2 u_i' + H_4 u_j' \tag{18}$$

$$v = H_2\varphi_i + H_4\varphi_j \tag{19}$$

where H_1, H_2, H_3 and H_4 are the Hermite cubic polynomials [32]. In the range of $0 \leq x \leq L_{k0}$, these functions are defined as

$$H_1 = 1 - 3\frac{x^2}{L^2} + 2\frac{x^3}{L^3} \tag{20}$$

$$H_2 = x - 2\frac{x^2}{L} + \frac{x^2}{L^2} \tag{21}$$

$$H_3 = 3\frac{x^2}{L^2} - 2\frac{x^3}{L^3} \tag{22}$$

$$H_4 = -\frac{x^2}{L} + \frac{x^3}{L^2} \tag{23}$$

With referring to the energy introduced in Sec. 3, we can write down the discretized form of the energy by calculating the single contribution due to every finite element and every pivot constituting the structure and by summing them. So we have for the stretching energy

$$w_{hs} = \frac{1}{2}\int_0^{L_h} EA\ \epsilon^2\, dx \quad h \in \{1, M\} \tag{24}$$

and for the bending energy

$$w_{hb} = \frac{1}{2}\int_0^{L_h} EI\ \kappa^2\, dx \quad h \in \{1, M\} \tag{25}$$

while the pivot torsion energy is

$$w_{hp} = \frac{1}{2}k_p\left(\frac{\pi}{2} - \Delta\alpha_h\right)^2 \quad h \in \{1, N_p - 4\} \tag{26}$$

and lastly the interaction energy is

$$w_{hf} = \frac{1}{2}k_f(\lambda_h^2 + k_3\lambda_h^3 + \dots) \quad h \in \{1, N_p - 4\} \tag{27}$$

The strain energy defined for each beam element of the pantographic sheet allows us to easily define the total strain energy by simply summing each contribution

$$W_s = \sum_{h=1}^{M} w_{hs} \tag{28}$$

for the stretching energy U_s of the structure,

$$W_b = \sum_{h=1}^{M} w_{hb} \tag{29}$$

for the bending energy U_b of the structure, and similarly for the two terms related to deformations of pivots

$$W_p = \sum_{h=1}^{N_p-4} w_{hp} \ , \quad W_f = \sum_{h=1}^{N_p-4} w_{hf} \tag{30}$$

Then we have

$$W = W_s + W_b + W_p + W_f \tag{31}$$

for the total energy W of the structure.

In order to have a complete solution of the considered equilibrium problem, displacements of nodes and forces exerted by each beam element on each other, a step-by-step optimization procedure was implemented to reconstruct the complete equilibrium path of the pantographic sheet, as it will be described in detail in the following. The generalized displacements of the grid nodes are collected in the vector $\boldsymbol{D} = \left\{\boldsymbol{U}_i, \boldsymbol{U}'_i, \boldsymbol{V}_i, \boldsymbol{\Phi}_i\right\}$, where $i = \{A, B\}$ for the two families of beams, in order to write the total energy of the pantographic structure in the form [12]

$$\Pi(\boldsymbol{D}) = W - L_{ext} \tag{32}$$

where

$$\boldsymbol{U}_i = \left\{U_{i1}, U_{i2}, \ldots, U_{iN_p}\right\} \tag{33}$$

$$\boldsymbol{U}'_i = \left\{U'_{i1}, U'_{i2}, \ldots, U'_{iN_p}\right\} \tag{34}$$

$$\boldsymbol{V}_i = \left\{V_{i1}, V_{i2}, \ldots, V_{iN_p}\right\} \tag{35}$$

$$\boldsymbol{\Phi}_i = \left\{\Phi_{i1}, \Phi_{i2}, \ldots, \Phi_{iN_p}\right\} \tag{36}$$

where L_{ext} is the work of the external loads and all quantities on the RHS depend on the variable $\boldsymbol{D}$. The displacements of a sub-set of nodes are imposed and external conservative forces are applied to the remaining sub-set of nodes. Thus, vector $\boldsymbol{D}$ can be decomposed into the pair of two sub-vectors: the imposed displacements $\boldsymbol{D}_a$ and the free displacements $\boldsymbol{D}_f$

$$\boldsymbol{D} = \{\boldsymbol{D}_a, \boldsymbol{D}_f\}$$

Obviously, L_{ext} is the work done by the external forces possibly applied to free degrees of freedom $\boldsymbol{D}_f$ of structural nodes. In particular, it is possible to impose the displacement directly and not an external force: in this case, as the one here analysed, we do not include L_{ext} in the optimization procedure. Moreover, the specification of suitable boundary conditions is needed where displacements are imposed, leading to the further decomposition of the sub-vector $\boldsymbol{D}_a$

$$\boldsymbol{D}_a = \{\boldsymbol{D}_{fix}, \boldsymbol{D}_{act}\} = \{\boldsymbol{0}, \boldsymbol{D}_{act}\} \tag{37}$$

in the sub-vector $\boldsymbol{D}_{fix}$ of fixed nodes and in the sub-vector of nodes, where a quasi-static loading condition

$$\boldsymbol{D}_{act} = \bar{\boldsymbol{D}} \tag{38}$$

consists of monotonically increasing displacements up to the maximum value $\bar{\boldsymbol{D}}$ applied to the actioned nodes.

5 Continuous non-linear Euler-Bernoulli beam theory

When the transition from the initial configuration $\mathcal{C}^*$ to the deformed $\mathcal{C}^t$ (stretched and deflected) configuration is characterized by finite displacements and rotations (Fig. 8) it is convenient to establish two abscissas, one of the undeformed configuration (x) and one of the deformed configuration (s), whereas $d\xi$ is the infinitesimal length of the rectilinear element connecting the ends of the curvilinear element in the deformed configuration. Also the angle $\theta(x)$ measures the rotation of the tangent line in any point (of abscissa x in the undeformed configuration) of the beam axis when the transition from undeformed to deformed shape takes place, Fig. 8.

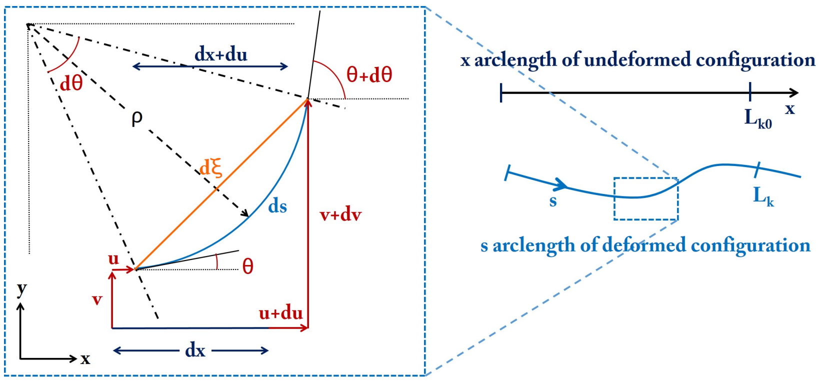

Fig. 8 Infinitesimal description of the beam in the actual configuration.

The infinitesimal length $d\xi$ of the current rectilinear element in the deformed beam is given by, Fig. 8,

$$d\xi^2 = (dx + du)^2 + dv^2 = [(1 + u')dx]^2 + dv^2 \tag{39}$$

$$d\xi = \sqrt{[(1 + u')dx]^2 + dv^2} \tag{40}$$

$$\frac{d\xi}{dx} = \sqrt{(1 + u')^2 + (v')^2} \tag{41}$$

where the convention $\frac{d(\cdot)}{dx} ='$ was adopted to indicate the derivation with respect to the x abscissa; u and v are the components of the displacement of the generic point of the beam axis, identified by the abscissa x. Therefore, the axial elongation is

$$\epsilon = \frac{ds - dx}{dx} \simeq \frac{d\xi - dx}{dx} = \sqrt{(1 + u')^2 + (v')^2} - 1 \tag{42}$$

According to [33], the curvature is defined as shown in Fig. 8

$$\frac{1}{\rho} = \kappa := \frac{d\theta}{ds} \simeq \frac{d\theta}{d\xi} \tag{43}$$

θ being defined as the angle which identifies the tangent

$$\psi = \tan\theta = \frac{dv}{dx + du} = \frac{v'}{1 + u'} \tag{44}$$

The rotation of the tangent line to the beam axis is

$$\theta = \arctan \psi \tag{45}$$

According to the equations (43) and (45), the curvature is given as

$$\kappa = \frac{d\theta}{d\xi} = \frac{d\theta}{dx} \cdot \frac{dx}{d\xi} = (\arctan \psi)' \frac{dx}{d\xi} \tag{46}$$

Moreover, equation (41) gives

$$\frac{dx}{d\xi} = \frac{1}{\sqrt{(1+u')^2 + (v')^2}} \tag{47}$$

Finally, observing that the derivative of the arctangent function is resolved as a noticeable derivative as

$$\frac{d\theta}{dx} = \frac{d}{dx} \arctan \psi = \frac{\psi'}{1+\psi^2} \tag{48}$$

yields the curvature with respect to the undeformed configuration

$$\kappa = \frac{\psi'}{1+\psi^2} \cdot \frac{1}{1+\epsilon} \tag{49}$$

where the definition of axial elongation of Eq. (42) has been used. The choice of this form of the curvature allows to account for stiffening due to positive stretching (length increment) of the beam axis. With the previous definitions we can derive the stretching energy for a beam of length L

$$W_s = \frac{1}{2} \int_0^L EA\epsilon^2 \, dx \tag{50}$$

and its bending energy.

$$W_b = \frac{1}{2} \int_0^L EI\kappa^2 \, dx \tag{51}$$

Throughout this paper, only material linearity is of interest. Thus, the sectional deformations are related to their conjugate-work sectional forces as follows:

$$N(x) = EA\epsilon \tag{52}$$

$$M(x) = EI\kappa \tag{53}$$

$$S(x) = \frac{dM}{dx} \cdot \frac{1}{1+\epsilon} = \frac{M'}{1+\epsilon} \tag{54}$$

where A, I are section's area and inertia moment, respectively, E is the Young's modulus, EA and EI are the axial and flexural rigidities, respectively, and $N(x)$, $M(x)$ and $S(x)$ are the section axial force, bending moment and shear force, respectively.

6 Basic modules

We now present two preliminary results obtained by using the algorithm previously described. The code needs as input the geometry of the pantograph (we give it by assigning the short side length ℓ and a parameter which is defined by the ratio with the long side L, $g = L/\ell$), the material characteristics and the loading conditions. For simplicity's sake, the interaction between the beams of the two orders occurs only by means of perfect internal hinges. The sample modules have X- and XX-shape, respectively.

The analysis of the two sample models and the presentation of the related results are important for demonstrating the validity of the modeling and the procedure proposed in this paper, as they allow (i) to evaluate in detail the capacity of the proposed method to take into account at the local level of element of the large displacements, rotations and deformations of the single beams and (ii) to make the operation of the procedure to be appreciate in terms of exchange between the two stretching and bending energy components. In fact, if on one hand the example with many degrees of freedom studied later in section 7 allows comparing the numerical results with the experimental ones under various aspects, it does not however make it easy, given its complexity, to consider local aspects of deformations and stress-resultants in the individual beam elements.

6.1 Basic grid X-module

As first example we consider the most simple pantographic structure, in which there are only two beams and one pivot in the intersection of the beams. This example was chosen to be able to observe in detail the behavior of the elemental grid mesh, a behavior that influences the overall behavior of the much more complex example studied in section 7. Table 3 shows the geometric, material and load data used in this example; Figure 9a shows the initial (undeformed) and final (deformed) configurations, as well as the numbering adopted for the nodes and for the elements. Figure 9b shows the progress of the two stretching and flexural energy components as the intensity of the applied external action increases, consisting in horizontal displacements impressed at the nodes 3 and 6. It is interesting to note the exchange point between the two components, where the stretching component exceeds the bending component, when the initially oblique fibers are aligning in the direction of the applied action.

Figure 10 shows the local deformation and stress characteristics in some particularly significant elements and nodes, as the intensity of the applied external action increases. In particular, Figure 10a shows the curvatures of the beams 3 and 4, Figure 10b shows the axial force and the shear force in the node 4 of the beam 3, Figure 10c shows the bending moment in the node 5 of the beam 3.

6.2 XX-module

In this subsection an intermediate example is studied between the basic example (X-module) analyzed in the previous section and the complex example studied in section 7. It consists of a double elemental mesh (XX-module). It has been chosen

System	two beams, four elements
Geometry ℓ g	 $0.007\,m$ 1
Sectional and material properties Cross-section area Cross-section inertia moment Youngs modulus	 $144 \cdot 10^{-8}\,m^2$ $12 \cdot 10^{-16}\,m^4$ $1600 \cdot 10^6\,Pa$
Displacement boundary conditions	Nodes 1 and 4 fixed
Loading condition Increment	Nodes 3 and 6 actioned horizontal displacement 20 steps $1 \cdot 10^{-4}\,m$

Table 3 Input for the basic grid X-module

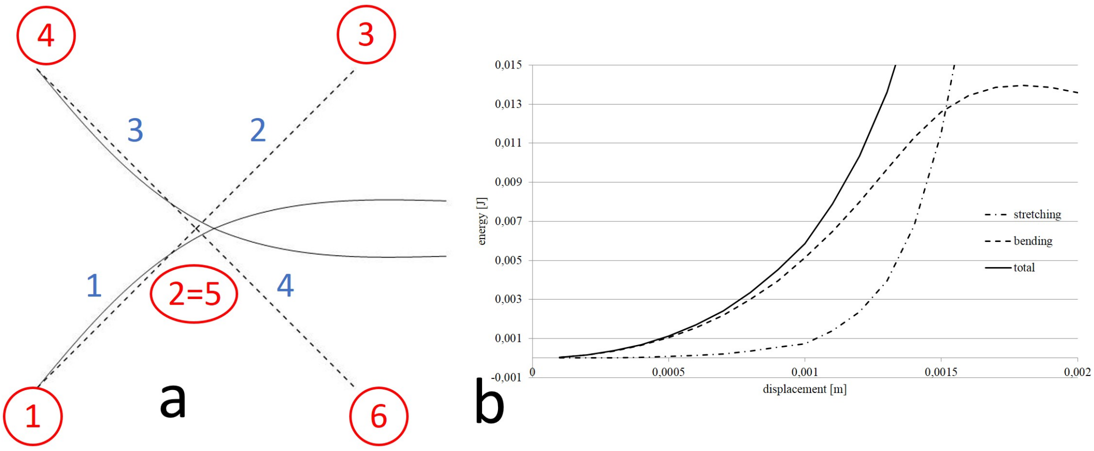

Fig. 9 (a) Basic module: referential form (dashed line), current form (solid line). (b) Strain energy.

because it allows us to verify the interactions in terms of deformation characteristics and stress-resultants between two elemental meshes at local level of nodes and elements, aspects which on the one hand can not obviously be highlighted by the isolated basic example and on the other do not stand out in the foreground in the example of section 7, veiled by its complexity.

Table 4 shows the geometric, material and load data used in this example; Figure 11 shows the initial (undeformed) and final (deformed) configurations, as well as the numbering adopted for the nodes and for the elements. Figure 12a shows the progress of the two stretching and flexural energy components as the intensity of the applied external action increases, consisting in horizontal displacements impressed at the nodes 1, 6, 7 and 12. It is also interesting to note also in this case the occurrence of the exchange point between the two components, where the stretching component exceeds the bending component, when the initially oblique fibers are aligning in the direction of the applied action.

Figure 12 shows the local deformation and stress characteristics in some particularly significant elements and nodes, as the intensity of the applied external

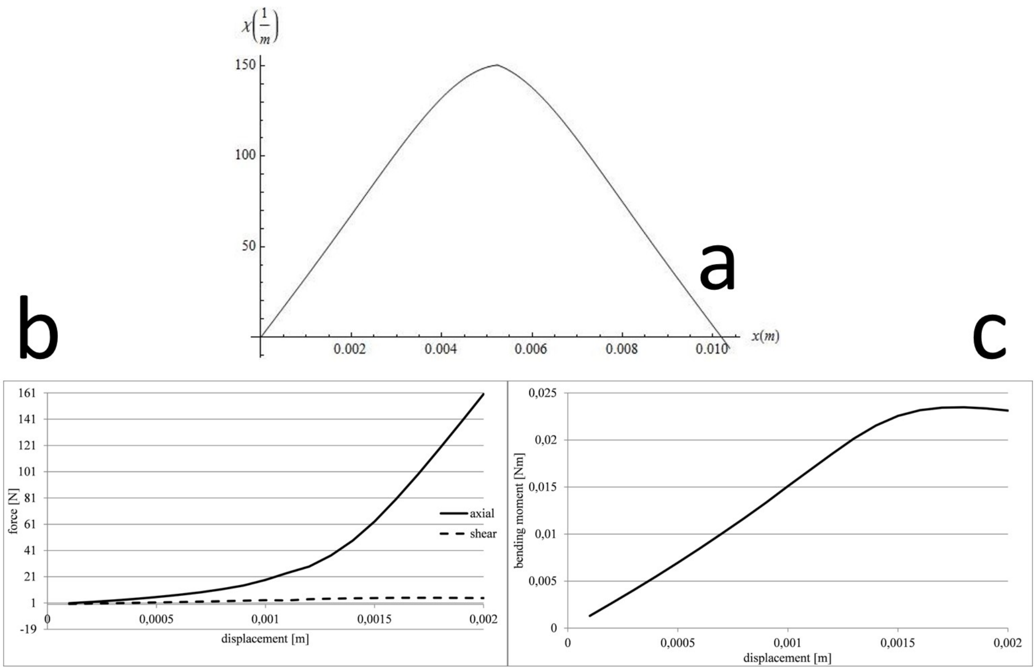

Fig. 10 (a) Beam curvature (elements 3 and 4). (b) Axial and shear forces (element 3, node 4). (c) Bending moment (element 3, node 5).

System	four beams, eight elements
Geometry ℓ g	 $70\,mm$ 3
Sectional and material properties Cross-section area Cross-section inertia moment Youngs modulus	 $144 \cdot 10^{-8}\,m^2$ $12 \cdot 10^{-16}\,m^4$ $1600 \cdot 10^6\,Pa$
Displacement boundary conditions	Nodes 1, 6, 7 and 12 vertically fixed
Loading condition Increment	Nodes 1, 6, 7 and 12 actioned horizontal displacement 18 steps $1 \cdot 10^{-4}\,m$

Table 4 Input for the XX-module

action increases. In particular, Figure 12b shows the curvatures of the beams 3 and 4, Figure 12c shows the axial force and the shear force in the node 3 of the beam 2, Figure 12d shows the bending moment in the node 2 of the beam 2.

7 Numerical simulations and comparison with experimental measures

We now can study the experimental problem, which is represented by the pantographic structure in Fig. 1. All the experimental relevant properties of the sample are given in Tab. 5

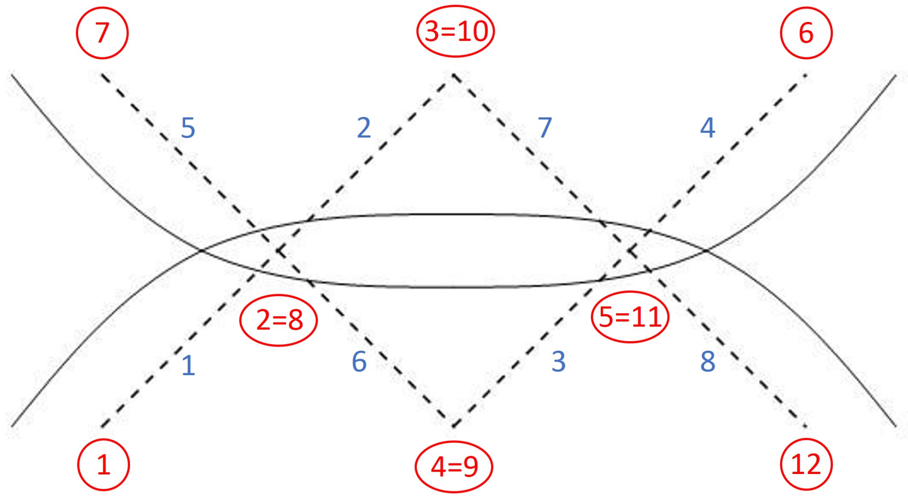

Fig. 11 XX structure: referential form (dashed line), current form (solid line).

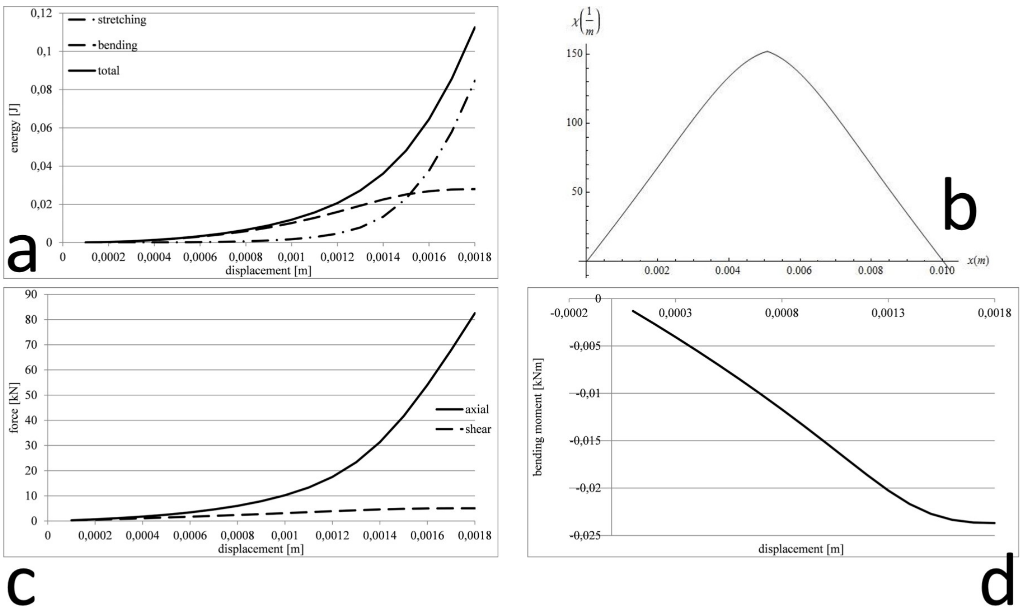

Fig. 12 (a) Strain energy. (b) Beam curvature (elements 3 and 4). (c) Axial and shear forces (element 2, node 3). (d) Bending moment (element 2, node 2).

The input data used for numerical simulation are reported in Tab. 6

By comparing the experimental force-displacement curve to the numerical one and the deformed shapes of the real sample to the ones obtained using the code we have identified the unknown rigidities k_p, k_f and k_3 in terms of a parameter ε,

Properties of the sample	
Material	Polyamide PA2200
ℓ	$70\,mm$
g	3
Pivot height	$3\,mm$
Pivot radius	$0.5\,mm$
ε	$1.53 \cdot 10^{-4}$
Unknown rigidities	
k_p	$30\varepsilon^2 N/m$
k_f	$8 \cdot 10^6 \varepsilon^2 N/m$
k_3	$1.8 \cdot 10^5 \varepsilon^2 N/m^2$

Table 5 Properties of the sample used in the experiment

System	30 beams, 96 elements
Geometry	
ℓ	$70\,mm$
g	3
Sectional and material properties	
Cross-section area	$144 \cdot 10^{-8}\,m^2$
Cross-section inertia moment	$9.72 \cdot 10^{-14}\,m^4$
Youngs modulus	$1600 \cdot 10^6\,Pa$
Displacement boundary conditions	Nodes of the right side vertically fixed
Loading condition	Nodes of the right side actioned horizontal displacement 20 steps
Increment	$2.85 \cdot 10^{-3}\,m$

Table 6 Input for the simulation of the experimental problem

that is related to the geometrical properties of the considered pantograph. Their numerical values are also listed in Tab. 5.

The first result we obtain is the energy in function of the imposed displacement (see Fig. 13); in particular, we can see the total energy and the simple contributions (stretching, bending, pivot torsion, interaction). From the Castigliano's Theorem, via a process of discrete derivation, we obtain a force-displacement relation. This relation is plotted in Fig. 14, in which we can see a comparison with the experimental data, represented by the continue line (which consists of an interpolation of the experimental points through third order polynomials). The dashed lines give an error band, which was obtained by considering the experimental noise (more bigger than the sensibility of the instrument of measure, which is $\approx 1N$).

Lastly we can compare the deformed shape of the pantograph obtained by the numerical minimization to the experimental one (see Fig.15). We also compare the measured values of the angles defined in Fig. 1 with their computed values (see Fig. 16). In Fig. 15 we can see four different shapes for four different displacement steps: in Fig. 15.a $\Delta U = 0.014\,m$, in Fig. 15.b $\Delta U = 0.037\,m$, in Fig. 15.c $\Delta U = 0.048\,m$ and in Fig. 15.d $\Delta U = 0.054\,m$, which corresponds to the maximum displacement reached before the first breakage.

In Tab. 7 we give the reaction forces exerted on the pivots of the right short side (see Fig. 17) for the maximum imposed displacement $\Delta U = 0.057\,m$ (the corresponding deformed shape is shown in Fig. 15.d). As it is well depicted both in table 7 and in figure 17, we have that the y-component of the reaction force is

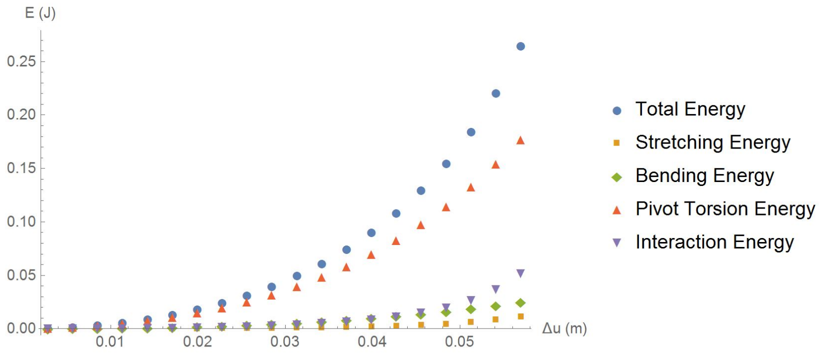

Fig. 13 Energy in function of the displacement.

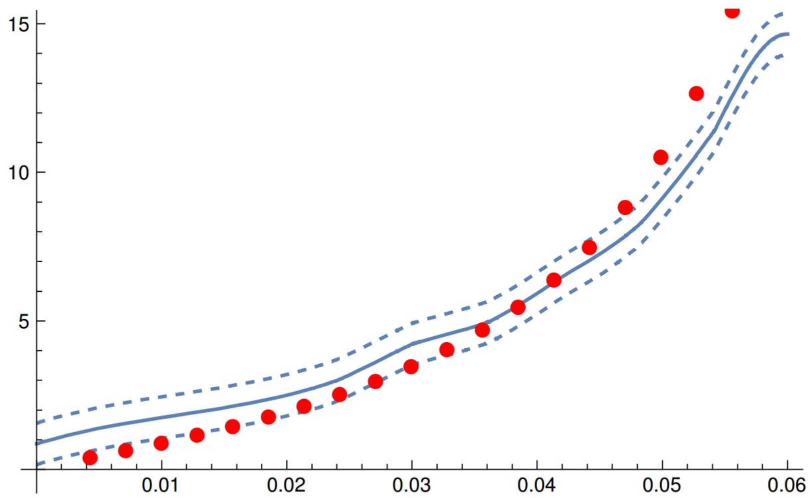

Fig. 14 Force-displacement curve. In grey the experimental data and in red the numerical simulation.

x component of reaction		y component of reaction	
R_{1x}	$9.04\,N$	R_{1y}	$9.13\,N$
R_{2x}	$1.66\,N$	R_{2y}	$0.47\,N$
R_{3x}	$0.12\,N$	R_{3y}	0.00
R_{4x}	$0.96\,N$	R_{4y}	$-0.51\,N$
R_{5x}	$9.12\,N$	R_{5y}	$-9.17\,N$

Table 7 Reaction forces exerted on the pivots of the right short side

emisymmetric distribution at null average, while the x-component is distributed in a *parabolic-like* way.

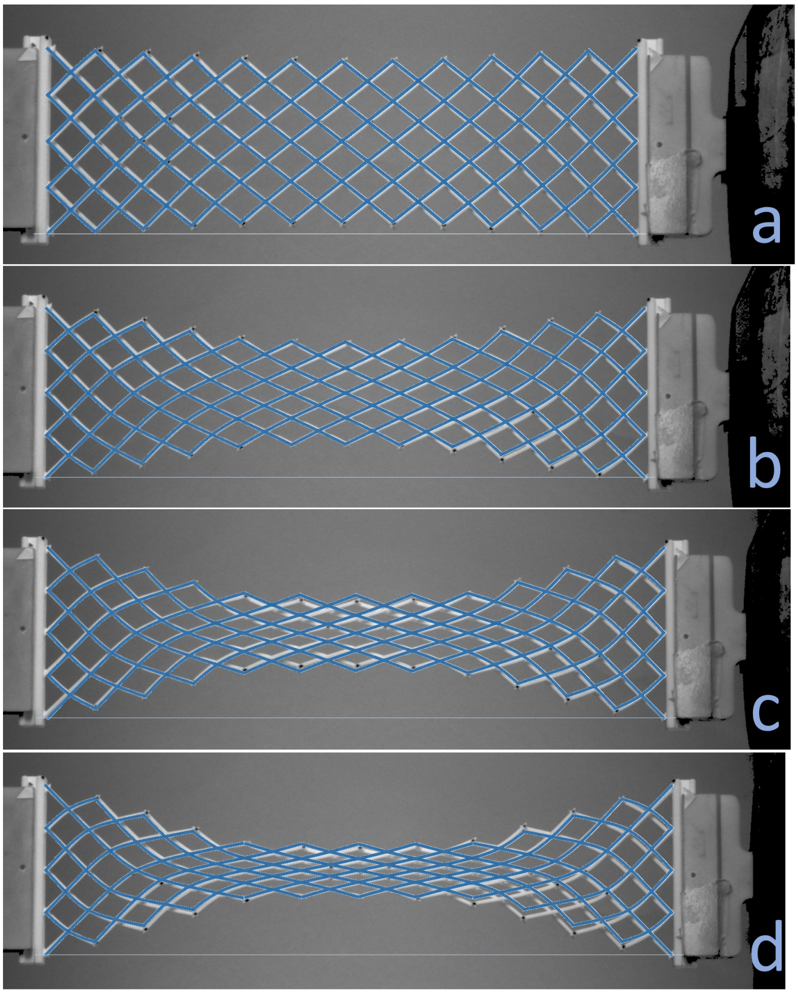

Fig. 15 Superposition of experimental (gray) and numerical (blue) shapes for four different displacements: (a) $0.014\,m$, (b) $0.037\,m$, (c) $0.048\,m$, (d) $0.054\,m$.

8 Discussion

The possibility given to the beams to slide one respect to the other in correspondence of the pivots theoretically allows us to qualitatively forecast the arising of fracture in the pantographic sheet.

As it is well known from the previous literature [34–39], fracture was observed predominantly in one of the corners of the sheet, because of the elongation energy stored in the angular beam. In [30] was firstly attempted to explain some phenomena of fracture in aluminum printed pantographs on the basis of the relative motion between the beams of the two different families.

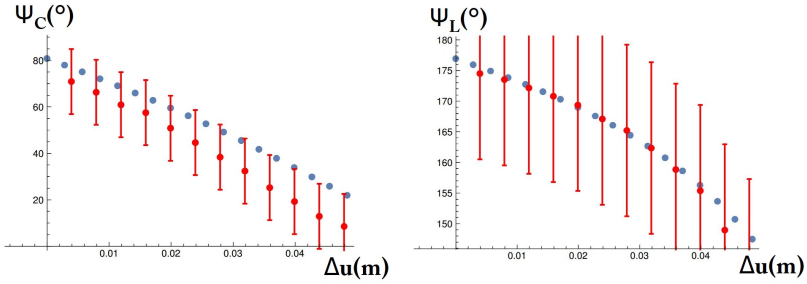

Fig. 16 Angles ψ_C and ψ_L. In red the experimental data with error bar given by the measure procedure and in blue the numerical simulation.

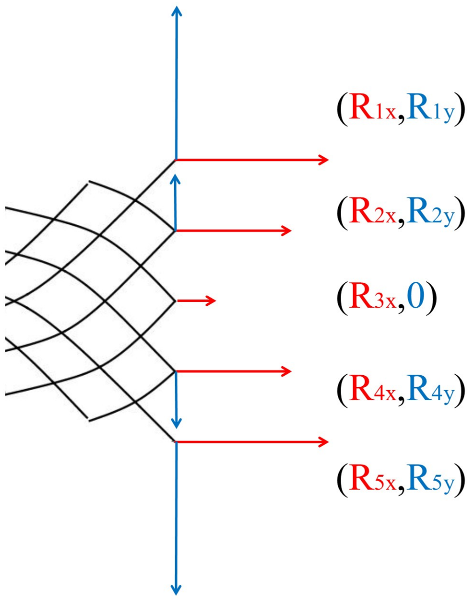

Fig. 17 Force reactions for every pivot in the side at which the displacement has been applied.

The algorithm here developed is able to forecast the onset of fracture, if the mechanism responsible for it is based on a threshold of the relative displacement. In Fig. 18 it is possible to see the relative displacement between beams as a 3D bar graph, plotted on the shape of the pantographic sheet: as it is clear from the figure, there are two maxima (an interesting aspect related to the introduction of the cubic factor in the *sliding* energetic term is the breaking of symmetry in the plot of relative displacement), which correspond to two precise pivots. One of them will undergo the first rupture, due to a flexural/shear stress. This is proven in Fig. 19, where a well explicative sequence showing the load step when the earlier fracture occurs is presented: the broken pivot is precisely the one forecasted by the model.

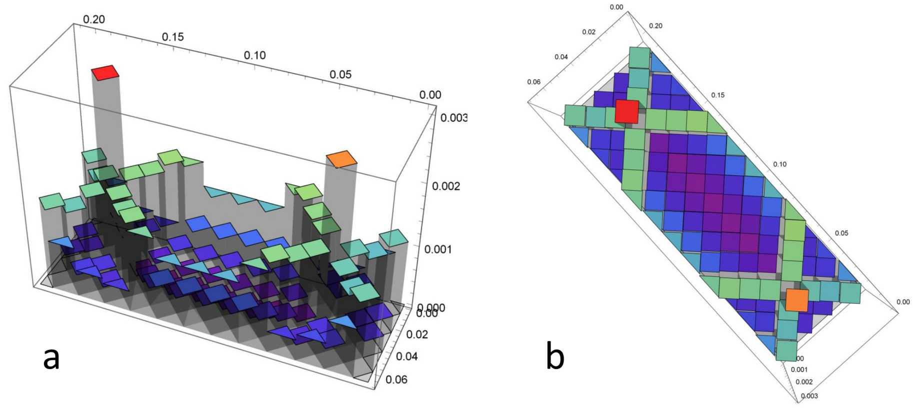

Fig. 18 Plot of the relative displacement on the shape of the pantographic sheet.

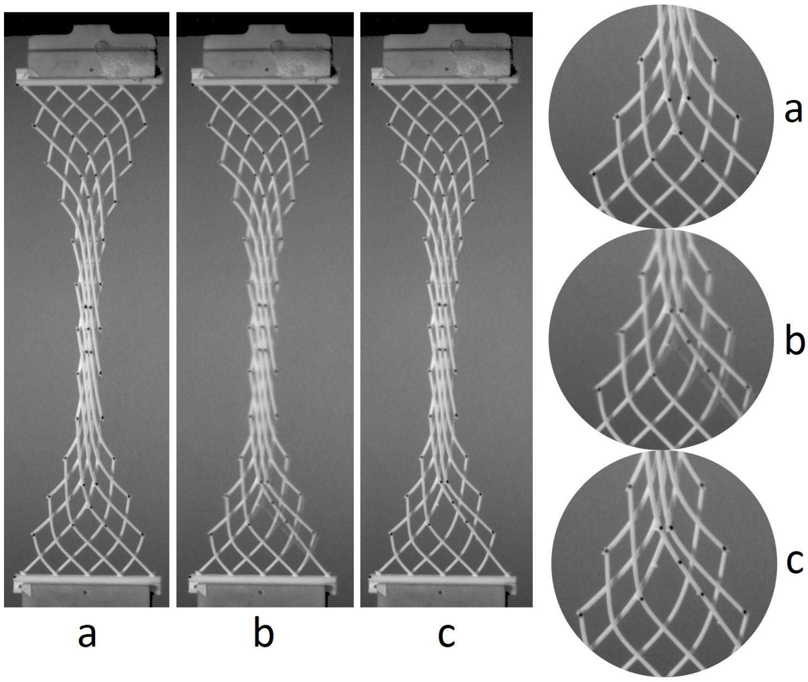

Fig. 19 A well explicative sequence which shows the moment of the first fracture, in the pivot forecasted by the model.

Some useful tools in modelling damage and fracture can be found in [40, 41]. From the information about the relative displacement we can forecast the onset of fracture, i.e. we can give a scheme of the weakest zones in the shape of the pantographic sheet: it could be useful, as it as been done in [42, 43], to consider the possibility of a shape/topology optimisation to obtain a stronger structure. The damage growth path can also be experimentally followed via some novel and very precise techniques of measure, as shown in [44,45]. The model of elastic-plastic planar frames and the incremental solution procedure presented in [46–49] can be considered as precursors of the above mentioned failure analysis of pantograph structures.

9 Conclusion

The advancement of 3D printing technologies allowed to realise relatively small structures constituted by beams and some elastic constraints [50,51]. If homogenised [52–55], these structures may lead to non-standard generalised continua. As usually remarked along the history of science, the feed-back from technological advancement opens new scientific perspectives and produces novel theoretical frameworks by changing paradigms [56–60]. This paper can be placed in the described scientific framework.

We have presented a computationally efficient and predictive model for a global analysis of the behaviour under deformation of pantographic structures. We have validated our model via comparison to some experimental measures. As an extension of the model presented in [1], aimed by some ideas studied in [61–65] and first applied in [30], we added a new energetic term to the potential energy owned by the pantographic structure and deriving from the possibility given to the beams of the two different families to slide one respect to the other in correspondence of the interconnecting pivot. From this new term, as we have shown in Sec. 8, we are able to forecast the onset of fracture when the fundamental mechanism responsible for it, as in our case, is based on a threshold of the relative displacement. Of course we can improve the efficiency of the here developed numerical tool: some possible improvements can be realised for example by using more performing methods, as isogeometrical analysis or conjugate gradient methods [66, 67].

The method here developed can be in future works generalised to treat some different structures, constituted for example by plates and shells [68, 69], or different beam theories [70] or eventually deformation tests (e.g. shear test as in [71]). In case a dynamical study need to be performed (we imagine, for example, the possibility to observe travelling waves around a pantographic sheet), useful tools about non-linear dynamics in fibres can be found in [72].

Acknowledgements This research was funded by the Italian Ministry of University and Research, under the Scientic Research Program of Relevant National Interest: Year 2010 2011, Protocol 2010MBJK5B-005, Title "Dynamics, Stability and Control of Flexible Structures".

Mario Spagnuolo has received funding from the European Union's Horizon 2020 research and innovation programme under the Marie Skłodowska-Curie grant agreement No 665850.

References

1. F. dell'Isola, I. Giorgio, M. Pawlikowski, and N. Rizzi, "Large deformations of planar extensible beams and pantographic lattices: heuristic homogenization, experimental and numerical examples of equilibrium," in *Proc. R. Soc. A*, vol. 472, no. 2185, 2016, p. 20150790.
2. A. M. Bersani, A. Della Corte, G. Piccardo, and N. L. Rizzi, "An explicit solution for the dynamics of a taut string of finite length carrying a traveling mass: the subsonic case," *Zeitschrift für angewandte Mathematik und Physik*, vol. 67, no. 4, p. 108, 2016.

3. A. Lazarus, C. Maurini, and S. Neukirch, “Stability of discretized nonlinear elastic systems,” in *Extremely Deformable Structures.* Springer, 2015, pp. 1–53.
4. L. Placidi, E. Barchiesi, E. Turco, and N. L. Rizzi, “A review on 2d models for the description of pantographic fabrics,” *Zeitschrift für angewandte Mathematik und Physik*, vol. 67, no. 5, p. 121, 2016.
5. L. Placidi, U. Andreaus, and I. Giorgio, “Identification of two-dimensional pantographic structure via a linear D4 orthotropic second gradient elastic model,” *Journal of Engineering Mathematics*, vol. 103, no. 1, pp. 1–21, 2017.
6. U. Andreaus, F. dell’Isola, I. Giorgio, L. Placidi, T. Lekszycki, and N. L. Rizzi, “Numerical simulations of classical problems in two-dimensional (non) linear second gradient elasticity,” *International Journal of Engineering Science*, vol. 108, pp. 34–50, 2016.
7. L. Placidi, L. Greco, S. Bucci, E. Turco, and N. L. Rizzi, “A second gradient formulation for a 2D fabric sheet with inextensible fibres,” *Zeitschrift für angewandte Mathematik und Physik*, vol. 67, no. 5, p. 114, 2016.
8. F. dell’Isola, I. Giorgio, and U. Andreaus, “Elastic pantographic 2D lattices: a numerical analysis on the static response and wave propagation,” *Proceedings of the Estonian Academy of Sciences*, vol. 64, no. 3, p. 219, 2015.
9. Di Carlo, A and Rizzi, N L and Tatone, A, “One-dimensional continuum model of a modular lattice: identification of the constitutive functions for the contact and inertial actions,” *Meccanica*, vol. 25, pp. 168–174, 1990.
10. F. dell’Isola, A. Della Corte, I. Giorgio, and D. Scerrato, “Pantographic 2D sheets: Discussion of some numerical investigations and potential applications,” *International Journal of Non-Linear Mechanics*, vol. 80, pp. 200–208, 2016.
11. F. dell’Isola, M. Cuomo, L. Greco, and A. Della Corte, “Bias extension test for pantographic sheets: numerical simulations based on second gradient shear energies,” *Journal of Engineering Mathematics*, vol. 103, no. 1, pp. 127–157, 2017.
12. E. Turco, F. dell’Isola, A. Cazzani, and N. L. Rizzi, “Hencky-type discrete model for pantographic structures: numerical comparison with second gradient continuum models,” *Zeitschrift für angewandte Mathematik und Physik*, vol. 67, no. 4, pp. 1–28, 2016.
13. E. Turco, F. dell’Isola, N. L. Rizzi, R. Grygoruk, W. H. Müller, and C. Liebold, “Fiber rupture in sheared planar pantographic sheets: Numerical and experimental evidence,” *Mechanics Research Communications*, vol. 76, pp. 86–90, 2016.
14. E. Turco and N. L. Rizzi, “Pantographic structures presenting statistically distributed defects: numerical investigations of the effects on deformation fields,” *Mechanics Research Communications*, vol. 77, pp. 65–69, 2016.
15. I. Giorgio, A. Della Corte, F. dell’Isola, and D. J. Steigmann, “Buckling modes in pantographic lattices,” *Comptes rendus Mecanique*, vol. 344, no. 7, pp. 487–501, 2016.
16. A. Battista, L. Rosa, R. dellErba, and L. Greco, “Numerical investigation of a particle system compared with first and second gradient continua: Deformation and fracture phenomena,” *Mathematics and Mechanics of Solids*, p. 1081286516657889, 2016.
17. A. Della Corte, A. Battista *et al.*, “Referential description of the evolution of a 2d swarm of robots interacting with the closer neighbors: perspectives of continuum modeling via higher gradient continua,” *International Journal of Non-Linear Mechanics*, vol. 80, pp. 209–220, 2016.
18. A. De Masi, I. Merola, E. Presutti, and Y. Vignaud, “Potts models in the continuum. uniqueness and exponential decay in the restricted ensembles,” *Journal of Statistical Physics*, vol. 133, no. 2, pp. 281–345, 2008.
19. ——, “Coexistence of ordered and disordered phases in potts models in the continuum,” *Journal of Statistical Physics*, vol. 134, no. 2, pp. 243–306, 2009.
20. S. Forest and K. Sab, “Finite-deformation second-order micromorphic theory and its relations to strain and stress gradient models,” *Mathematics and Mechanics of Solids*, p. 1081286517720844, 2017.
21. Z.-P. Wang, L. H. Poh, J. Dirrenberger, Y. Zhu, and S. Forest, “Isogeometric shape optimization of smoothed petal auxetic structures via computational periodic homogenization,” *Computer Methods in Applied Mechanics and Engineering*, vol. 323, pp. 250–271, 2017.
22. A. Javili and P. Steinmann, “A finite element framework for continua with boundary energies. part i: The two-dimensional case,” *Computer Methods in Applied Mechanics and Engineering*, vol. 198, no. 27, pp. 2198–2208, 2009.
23. A. Javili, F. dell’Isola, and P. Steinmann, “Geometrically nonlinear higher-gradient elasticity with energetic boundaries,” *Journal of the Mechanics and Physics of Solids*, vol. 61, no. 12, pp. 2381–2401, 2013.

24. N. Auffray, J. Dirrenberger, and G. Rosi, “A complete description of bi-dimensional anisotropic strain-gradient elasticity,” *International Journal of Solids and Structures*, vol. 69, pp. 195–206, 2015.
25. V. A. Eremeyev, “On equilibrium of a second-gradient fluid near edges and corner points,” in *Advanced Methods of Continuum Mechanics for Materials and Structures.* Springer, 2016, pp. 547–556.
26. F. dell'Isola and P. Seppecher, “The relationship between edge contact forces, double forces and interstitial working allowed by the principle of virtual power,” *Comptes rendus de lAcadémie des sciences. Série IIb, Mécanique, physique, astronomie*, p. 7, 1995.
27. P. Seppecher, J.-J. Alibert, and F. dell'Isola, “Linear elastic trusses leading to continua with exotic mechanical interactions,” in *Journal of Physics: Conference Series*, vol. 319, no. 1. IOP Publishing, 2011, p. 012018.
28. F. dell'Isola and P. Seppecher, “Edge contact forces and quasi-balanced power,” *Meccanica*, vol. 32, no. 1, pp. 33–52, 1997.
29. A. Madeo, A. Della Corte, L. Greco, and P. Neff, “Wave propagation in pantographic 2D lattices with internal discontinuities,” *Proceedings of the Estonian Academy of Sciences*, vol. 64, no. 3S, pp. 325–330, 2015.
30. M. Spagnuolo, K. Barcz, A. Pfaff, F. dell'Isola, and P. Franciosi, “Qualitative pivot damage analysis in aluminum printed pantographic sheets: numerics and experiments,” *Mechanics Research Communications*, vol. 83, pp. 47–52, 2017.
31. T. N. Le, J.-M. Battini, and M. Hjiaj, “Co-rotational dynamic formulation for 2D beams,” in *COMPDYN 2011 3rd International Conference on Computational Methods in Structural Dynamics & Earthquake Engineering, Corfu, Greece, 2011*, 2011.
32. R. D. Cook, D. S. Malkus, M. E. Plesha, and R. J. Witt, *Concepts and applications of finite element analysis.* Wiley New York, 1974, vol. 4.
33. R. Baldacci, *Scienza delle Costruzioni.* UTET, Torino, 1997, vol. I.
34. E. Turco, K. Barcz, M. Pawlikowski, and N. L. Rizzi, “Non-standard coupled extensional and bending bias tests for planar pantographic lattices. part I: numerical simulations,” *Zeitschrift für angewandte Mathematik und Physik*, vol. 67, no. 5, p. 122, 2016.
35. E. Turco, K. Barcz, and N. L. Rizzi, “Non-standard coupled extensional and bending bias tests for planar pantographic lattices. part II: comparison with experimental evidence,” *Zeitschrift für angewandte Mathematik und Physik*, vol. 67, no. 5, p. 123, Sep 2016.
36. F. dell'Isola, A. Della Corte, L. Greco, and A. Luongo, “Plane bias extension test for a continuum with two inextensible families of fibers: A variational treatment with Lagrange multipliers and a perturbation solution,” *International Journal of Solids and Structures*, vol. 81, pp. 1–12, 2016.
37. M. Cuomo, F. dell'Isola, and L. Greco, “Simplified analysis of a generalized bias test for fabrics with two families of inextensible fibres,” *Zeitschrift für angewandte Mathematik und Physik*, vol. 67, no. 3, p. 61, 2016.
38. M. Cuomo, F. dell'Isola, L. Greco, and N. Rizzi, “First versus second gradient energies for planar sheets with two families of inextensible fibres: Investigation on deformation boundary layers, discontinuities and geometrical instabilities,” *Composites Part B: Engineering*, vol. 115, pp. 423–448, 2017.
39. E. Turco, M. Golaszewski, A. Cazzani, and N. L. Rizzi, “Large deformations induced in planar pantographic sheets by loads applied on fibers: experimental validation of a discrete lagrangian model,” *Mechanics Research Communications*, vol. 76, pp. 51–56, 2016.
40. J.-J. Marigo, C. Maurini, and K. Pham, “An overview of the modelling of fracture by gradient damage models,” *Meccanica*, vol. 51, no. 12, pp. 3107–3128, 2016.
41. N. Challamel, C. Lanos, and C. Casandjian, “Strain-based anisotropic damage modelling and unilateral effects,” *International journal of mechanical sciences*, vol. 47, no. 3, pp. 459–473, 2005.
42. A. Catapano, B. Desmorat, and P. Vannucci, “Invariant formulation of phenomenological failure criteria for orthotropic sheets and optimisation of their strength,” *Mathematical Methods in the Applied Sciences*, vol. 35, no. 15, pp. 1842–1858, 2012.
43. B. Desmorat and R. Desmorat, “Topology optimization in damage governed low cycle fatigue,” *Comptes Rendus Mecanique*, vol. 336, no. 5, pp. 448–453, 2008.
44. A. Carpiuc-Prisacari, M. Poncelet, K. Kazymyrenko, F. Hild, and H. Leclerc, “Comparison between experimental and numerical results of mixed-mode crack propagation in concrete: Influence of boundary conditions choice,” *Cement and Concrete Research*, vol. 100, pp. 329–340, 2017.

45. A. Doitrand, C. Fagiano, F. Hild, V. Chiaruttini, A. Mavel, and M. Hirsekorn, "Mesoscale analysis of damage growth in woven composites," *Composites Part A: Applied Science and Manufacturing*, vol. 96, pp. 77–88, 2017.
46. U. Andreaus and A. Sawczuk, "Deflection of elastic-plastic frames at finite spread of yielding zones," *Computer Methods in Applied Mechanics and Engineering*, vol. 39, no. 1, pp. 21–35, 1983.
47. U. Andreaus and P. D'Asdia, "Displacement analysis in elastic-plastic frames at plastic collapse," *Computer methods in applied mechanics and engineering*, vol. 42, no. 1, pp. 19–35, 1984.
48. ——, "Incremental analysis of elastic-plastic frames at finite spread of yielding zones," *Engineering fracture mechanics*, vol. 21, no. 4, pp. 827–839, 1985.
49. ——, "An incremental procedure for deformation analysis of elastic-plastic frames," *International journal for numerical methods in engineering*, vol. 26, no. 4, pp. 769–784, 1988.
50. F. dell'Isola, T. Lekszycki, M. Pawlikowski, R. Grygoruk, and L. Greco, "Designing a light fabric metamaterial being highly macroscopically tough under directional extension: first experimental evidence," *Zeitschrift für angewandte Mathematik und Physik*, vol. 66, no. 6, pp. 3473–3498, 2015.
51. F. dell'Isola, D. Steigmann, and A. Della Corte, "Synthesis of fibrous complex structures: designing microstructure to deliver targeted macroscale response," *Applied Mechanics Reviews*, vol. 67, no. 6, p. 060804, 2015.
52. Y. Rahali, I. Giorgio, J. Ganghoffer, and F. dell'Isola, "Homogenization à la Piola produces second gradient continuum models for linear pantographic lattices," *International Journal of Engineering Science*, vol. 97, pp. 148–172, 2015.
53. J.-J. Alibert and A. Della Corte, "Second-gradient continua as homogenized limit of pantographic microstructured plates: a rigorous proof," *Zeitschrift für angewandte Mathematik und Physik*, vol. 66, no. 5, pp. 2855–2870, 2015.
54. C. Pideri and P. Seppecher, "A second gradient material resulting from the homogenization of an heterogeneous linear elastic medium," *Continuum Mechanics and Thermodynamics*, vol. 9, no. 5, pp. 241–257, 1997.
55. S. Forest and D. K. Trinh, "Generalized continua and non-homogeneous boundary conditions in homogenisation methods," *ZAMM-Journal of Applied Mathematics and Mechanics/Zeitschrift für Angewandte Mathematik und Mechanik*, vol. 91, no. 2, pp. 90–109, 2011.
56. F. dell'Isola, A. Della Corte, R. Esposito, and L. Russo, "Some cases of unrecognized transmission of scientific knowledge: from antiquity to gabrio piolas peridynamics and generalized continuum theories," in *Generalized continua as models for classical and advanced materials*. Springer, 2016, pp. 77–128.
57. L. Russo, *The forgotten revolution: how science was born in 300 BC and why it had to be reborn*. Springer Science & Business Media, 2013.
58. F. dell'Isola, S. Bucci, and A. Battista, "Against the Fragmentation of Knowledge: The Power of Multidisciplinary Research for the Design of Metamaterials," in *Advanced Methods of Continuum Mechanics for Materials and Structures*. Springer, 2016, pp. 523–545.
59. S. R. Eugster and F. dell'Isola, "Exegesis of the Introduction and Sect. I from Fundamentals of the Mechanics of Continua** by E. Hellinger," *ZAMM-Journal of Applied Mathematics and Mechanics/Zeitschrift für Angewandte Mathematik und Mechanik*, vol. 97, no. 4, pp. 477–506, 2017.
60. ——, "Exegesis of Sect. II and III. A from Fundamentals of the Mechanics of Continua** by E. Hellinger," *ZAMM-Journal of Applied Mathematics and Mechanics/Zeitschrift für Angewandte Mathematik und Mechanik*, 2017.
61. P. Franciosi and A. El Omri, "Effective properties of fiber and platelet systems and related phase arrangements in n-phase heterogenous media," *Mechanics Research Communications*, vol. 38, no. 1, pp. 38–44, 2011.
62. P. Franciosi, "Laminate system schemes for effective property estimates of architectured composites with co-(dis) continuous phases," *Mechanics Research Communications*, vol. 45, pp. 70–76, 2012.
63. ——, "The boundary-due terms in the green operator of inclusion patterns from distant to contact and to connected situations using radon transforms: Illustration for spheroid alignments in isotropic media," *International Journal of Solids and Structures*, vol. 47, no. 2, pp. 304–319, 2010.

64. P. Franciosi, S. Barboura, and Y. Charles, "Analytical mean green operators/eshelby tensors for patterns of coaxial finite long or flat cylinders in isotropic matrices," *International Journal of Solids and Structures*, vol. 66, pp. 1–19, 2015.
65. P. Franciosi, "Mean and axial green and eshelby tensors for an inclusion with finite cylindrical 3d shape," *Mechanics Research Communications*, vol. 59, pp. 26–36, 2014.
66. A. Cazzani, M. Malagù, and E. Turco, "Isogeometric analysis of plane-curved beams," *Mathematics and Mechanics of Solids*, vol. 21, no. 5, pp. 562–577, 2016.
67. A. Cazzani, M. Malagù, E. Turco, and F. Stochino, "Constitutive models for strongly curved beams in the frame of isogeometric analysis," *Mathematics and Mechanics of Solids*, vol. 21, no. 2, pp. 182–209, 2016.
68. J. Altenbach, H. Altenbach, and V. A. Eremeyev, "On generalized cosserat-type theories of plates and shells: a short review and bibliography," *Archive of Applied Mechanics*, vol. 80, no. 1, pp. 73–92, 2010.
69. V. Eremeyev, H. Altenbach, and N. Morozov, "The influence of surface tension on the effective stiffness of nanosize plates," in *Doklady Physics*, vol. 54, no. 2. Springer, 2009, pp. 98–100.
70. H. Altenbach, M. Bîrsan, and V. A. Eremeyev, "Cosserat-type rods," in *Generalized Continua from the Theory to Engineering Applications*. Springer, 2013, pp. 179–248.
71. D. Scerrato, I. A. Zhurba Eremeeva, T. Lekszycki, and N. L. Rizzi, "On the effect of shear stiffness on the plane deformation of linear second gradient pantographic sheets," *ZAMM-Journal of Applied Mathematics and Mechanics/Zeitschrift für Angewandte Mathematik und Mechanik*, vol. 96, no. 11, pp. 1268–1279, 2016.
72. A. Goriely and M. Tabor, "Nonlinear dynamics of filaments ii. nonlinear analysis," *Physica D: Nonlinear Phenomena*, vol. 105, no. 1-3, pp. 45–61, 1997.